

Role of symmetry in antiferromagnetic topological insulators

Sahar Ghasemi and Morad Ebrahimkhas

Citation: Chin. Phys. B, 2025, 34 (**7**): 077302. DOI: 10.1088/1674-1056/adcb1e
http://cpb.iphy.ac.cn; http://iopscience.iop.org/cpb

What follows is a list of articles you may be interested in

Random flux manipulating topological phase transitions in Chern insulators

Jinkun Wang(王锦坤) and Wu-Ming Liu(刘伍明)
Chin. Phys. B, 2025, 34 (**6**): 067301. DOI: 10.1088/1674-1056/adc36a

First principles prediction of the valley Hall effect in ScBrCl monolayer

Xiang Yu(于翔), Ping Li(李萍), and Chang-Wen Zhang(张昌文)
Chin. Phys. B, 2025, 34 (**4**): 047305. DOI: 10.1088/1674-1056/adbacb

Intrinsic valley-polarized quantum anomalous Hall effect in a two-dimensional germanene/MnI_2 van der Waals heterostructure

Xiao-Jing Dong(董晓晶) and Chang-Wen Zhang(张昌文)
Chin. Phys. B, 2024, 33 (**7**): 077303. DOI: 10.1088/1674-1056/ad4bbd

Identifying anomalous Floquet edge modes via bulk-edge correspondence

Huanyu Wang(王寰宇), Wuming Liu(刘伍明)
Chin. Phys. B, 2020, 29 (**4**): 047301. DOI: 10.1088/1674-1056/ab6dcb

Multi-carrier transport in $ZrTe_5$ film

Fangdong Tang(汤方栋), Peipei Wang(王培培), Peng Wang(王鹏), Yuan Gan(甘远), Le Wang(王乐), Wei Zhang(张威), Liyuan Zhang(张立源)
Chin. Phys. B, 2018, 27 (**8**): 087307. DOI: 10.1088/1674-1056/27/8/087307

Role of symmetry in antiferromagnetic topological insulators

Sahar Ghasemi[1] and Morad Ebrahimkhas[1,2,†]

[1] *Department of Physics, Mahabad Branch, Islamic Azad University, Mahabad, Iran*
[2] *Institut für Theoretische Physik, Goethe-Universität,* 60438 *Frankfurt/Main, Germany*

(Received 20 January 2025; revised manuscript received 23 March 2025; accepted manuscript online 10 April 2025)

In this investigation, we delve into the interplay between strong interactions and intricate topological configurations, leading to emergent quantum states such as magnetic topological insulators. The crux of our research centers on elucidating how lattice symmetry modulates antiferromagnetic quantum Hall phenomena. Utilizing the spinful Harper-Hofstadter model enriched with a next-nearest-neighbor (NNN) hopping term, we discern a half-filling bandgap, paving the way for the manifestation of a quantum Hall insulator characterized by a Chern number, $C = 2$. Upon integrating a checkerboard-patterned staggered potential (Δ) and the Hubbard interaction (U), the system exhibits complex dynamical behaviors. Marginal NNN hopping culminates in a Neél antiferromagnetic Mott insulator. In contrast, intensified hopping results in stripe antiferromagnetic configurations. Moreover, in the regime of limited NNN hopping, a $C = 1$ Neél antiferromagnetic quantum Hall insulator emerges. A salient observation pertains to the manifestation of a $C = 1$ antiferromagnetic quantum Hall insulator when spin-flip mechanisms are not offset by space group symmetries. These findings chart a pathway for further explorations into antiferromagnetic Quantum Hall States.

Keywords: antiferromagnetic quantum hall insulator, topological phase transitions, Harper–Hofstadter–Hubbard model, lattice symmetry effects

PACS: 73.43.–f, 71.27.+a, 75.10.–b

DOI: 10.1088/1674-1056/adcb1e **CSTR:** 32038.14.CPB.adcb1e

1. Introduction

The experimental advancements in generating artificial gauge fields[1,2] and in identifying magnetic order[3,4] propose that ultracold atoms confined in optical lattices[5] serve as an unparalleled system to emulate magnetic topological quantum states, offering significant control and adjustability of parameters. This study centers on ultracold atoms confined within optical lattices, serving as versatile platforms for controlled quantum simulations. These lattices offer a means to explore the properties of solid-state materials across diverse parameter regimes.[6–8] The strategic deployment of the Feshbach resonance effect allows for precise tuning of interaction strength and characteristics among ultracold atoms, spanning a broad spectrum.[9] In optical lattice systems, it becomes feasible to adjust both nearestneighbor (NN) and nextnearestneighbor (NNN) magnitudes, fostering tunable control. Notably, recent advancements highlight the feasibility of manipulating the $t_{\rm NNN}/t_{\rm NN} \equiv t'/t$ ratio through shaking techniques, thereby engendering a renormalization of hopping parameters.[10–14]

The investigation delves into the realm of condensed matter physics, particularly in the context of tight-binding models situated on two-dimensional square and honeycomb lattices subjected to a magnetic field.[15,16] Herein, the influence of hopping parameters is thoroughly explored. This domain encompasses the inclusion of Hubbard interaction and on-site potential terms,[17,18] enabling the analysis of phase diagrams and physical properties within these systems. Importantly, topological phase transitions are catalyzed by manipulation of the t'/thopping ratios,[19,20] along with adjustments to other potential components. Within this context, Ref. [20] discusses the orchestration of topological phase transitions through NNN hopping manipulation in structures such as the Lieb, kagome and T3 lattices.

While previous studies have primarily focused on the Haldane–Hubbard model for investigating interaction-driven topological phases, our work extends the analysis to the Harper–Hofstadter–Hatsugai–Hubbard (HHHH) model. This model includes a uniform magnetic flux and allows a more general investigation of symmetry effects on the stabilization of antiferromagnetic quantum Hall insulators (AFQHIs). Our results provide new insights into how explicit and spontaneous symmetrybreaking conditions affect the emergence of the $C = 1$ phase.

This research embarks on an exploration into whether the emergence of the $C = 1$ AFQHI is an exclusive attribute of the HaldaneHubbard model or extends to other interacting topological systems. To address this query, we delve into the spinful Harper-Hofstadter model augmented with Hubbard interaction (U), termed the Harper–Hofstadter–Hubbard model. Focusing on half-filling conditions and a plaquette magnetic flux of $1/2$ in units of magnetic flux quantum h/e, it is essential to note that this flux is uniform across both spin components. While the Harper-Hofstadter model at half-

†Corresponding author. E-mail: ebrahimkhas@gmail.com

© 2025 Chinese Physical Society and IOP Publishing Ltd. All rights, including for text and data mining, AI training, and similar technologies, are reserved.

filling lacks a gap, the introduction of NNN hopping instigates gap formation, thereby realizing a quantum Hall insulator (QHI) with a Chern number $C = 2$.[21] The emergence of the $C = 1$ AFQHI within the Haldane–Hubbard model stems from the interplay between the staggered potential and Hubbard interaction.[22–24] In our model, a staggered potential Δ favors a normal insulator (NI). The significance of symmetry in the evolution of contemporary condensed matter physics, particularly concerning topological insulators (TIs), is undeniably acknowledged. We argue that an antiferromagnetic QHI with a value of $C = 1$ can only arise when the impact of a spin-flip transformation is not offset by a space group action.

To gain insights into the system's topological properties, we harness real-space dynamical mean field theory (DMFT) as a formidable analytical tool. As an impurity solver, exact diagonalization (ED) is adeptly employed. These methodologies have found extensive application in the study of 2D lattices and topological insulators.[25–28] The exposition unfolds by introducing the HHHH Hamiltonian for the square lattice, followed by an in-depth elucidation of the real-space DMFT method. Subsequently, we delve into the application of the topological Hamiltonian method within an interacting regime, leading to an analysis of system topological properties and the construction of the topological phase diagram. A central aim is to interrogate the repercussions of tuning the t'/tratio, transitioning from weak to strong NNN hopping, and exploring the ensuing transformations in magnetic order.

2. Hamiltonian

We examine the HHHH Hamiltonian of the following form:

$$\begin{aligned} H \;=\; & -t\sum_{\boldsymbol{r},\sigma}\left(c^{\dagger}_{\boldsymbol{r}+\boldsymbol{x},\sigma}c_{\boldsymbol{r},\sigma}+\mathrm{e}^{2\pi\mathrm{i}\varphi}c^{\dagger}_{\boldsymbol{r}+\boldsymbol{y},\sigma}c_{\boldsymbol{r},\sigma}+\mathrm{h.c.}\right) \\ & -t'\sum_{\boldsymbol{r},\sigma}\left[\mathrm{e}^{2\pi\mathrm{i}\varphi\left(x+\frac{1}{2}\right)}\left(c^{\dagger}_{\boldsymbol{r}+\boldsymbol{y}+\boldsymbol{x},\sigma}c_{\boldsymbol{r},\sigma}+c^{\dagger}_{\boldsymbol{r}+\boldsymbol{y},\sigma}c_{\boldsymbol{r}+\boldsymbol{x},\sigma}\right)\right. \\ & \left.+\mathrm{h.c.}\right]+\Delta\sum_{\boldsymbol{r},\sigma}(-1)^{x+y}n_{\boldsymbol{r},\sigma}+U\sum_{\boldsymbol{r}}n_{\boldsymbol{r}\downarrow}n_{\boldsymbol{r},\uparrow}, \end{aligned} \tag{1}$$

here, t represents nearest neighbor hopping and t' stands for the NNN hopping. The operators $c^{\dagger}_{\boldsymbol{r},\sigma}(c_{\boldsymbol{r},\sigma})$ create (annihilate) particles at position $\boldsymbol{r} := (x,y)$ with flavor $\sigma := (\uparrow,\downarrow)$. The position $\boldsymbol{r}$ covers the square lattice with the lattice constant serving as the unit length. The occupation operator is defined as $n_{\boldsymbol{r},\sigma}$. We adopt a constant effective flux $\varphi = 1/2$ in this manuscript. The introduction of the complex hopping term is realized through an artificial gauge-field method, a technique extensively employed in the context of ultracold atoms within optical lattices.[29] The third term encompasses a staggered potential ($\pm\Delta$) alternating in checkerboard form, while the fourth term, U, represents the Hubbard repulsion potential.

The interplay between U and Δ critically influences the phase transition of this model. Additionally, the parameters φ and t'/t exert significant effects on the model's phase nature. Notably, the intriguing aspect of this Hamiltonian lies in the inclusion of a complex hopping term, wherein particles accumulate a fixed phase upon hopping. Figure 1 visually illustrates the Hamiltonian terms. The NN hopping parameters in the x direction between $A \to B$ sub-lattices are real and denoted as t. The NN hopping term in the y direction involves a complex value between atoms within distinct sub-lattices. The diagonals in Fig. 1 represent the complex NNN hopping between the same sub-lattices.

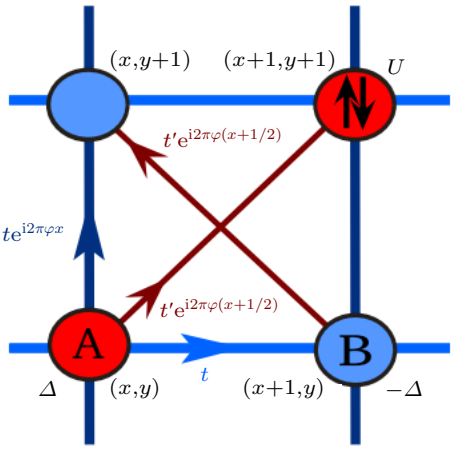


Fig. 1. Schematic representation of the Hamiltonian on the square lattice with NN, NNN hopping, U, and ionic potentials. The lattice comprises two sub-lattices, A and B, featuring opposite staggered potentials ($\pm\Delta$).

3. Method

The real-space dynamical mean field theory (RDMFT) has emerged as a potent tool applied extensively across diverse physical scenarios, including investigations of finite layers,[30] disordered systems,[31,32] unconventional magnetism,[33,34] and topological insulators.[27,28] RDMFT finds preference over the conventional DMFT approach in the study of ultracold atoms within optical lattices. This distinction arises from the local and position-dependent nature of the self-energy $\Sigma(\mathrm{i}\omega n)$ in the RDMFT, compared to the strictly local character of the DMFT.[35–37]

The self-consistency cycle within the RDMFT method unfolds as follows:

(i) The cycle commences with an initial estimation of the self-energy.

(ii) By employing the Dyson equation, one computes the lattice Green function $\boldsymbol{G}(\mathrm{i}\omega n)$, which can be expressed as:

$$G(\mathrm{i}\omega n) = \left[\mathrm{i}\omega n I - H_0 - \Sigma(\mathrm{i}\omega n)\right]^{-1}, \tag{2}$$

where the matrix elements of H_0 are defined as:

$$[H_0]_{\boldsymbol{r}\alpha,\boldsymbol{r}'\alpha'} = \left\langle \boldsymbol{r}\alpha \left| H \right| \boldsymbol{r}'\alpha' \right\rangle. \tag{3}$$

(iii) The local Green function, denoted as $G\boldsymbol{r}(\mathrm{i}\omega n)$, is deduced using Eq. (2):

$$\left[G_{\boldsymbol{r}}(\mathrm{i}\omega n)\right]_{\alpha,\alpha'} := \left[G(\mathrm{i}\omega n)\right]_{\boldsymbol{r}\alpha,\boldsymbol{r}'\alpha'}. \tag{4}$$

(iv) Employing the local Dyson equation, the inverse dynamical Weiss field is calculated:

$$\boldsymbol{G}(0)_{\boldsymbol{r}}(\mathrm{i}\omega n)^{-1} = \boldsymbol{G}_{\boldsymbol{r}}(\mathrm{i}\omega n)^{-1} + \boldsymbol{\Sigma}_{\boldsymbol{r}}(\mathrm{i}\omega n), \tag{5}$$

where the self-energy is expressed using the local property, $[\Sigma(\mathrm{i}\omega n)]_{\alpha,\alpha'} = \delta_{\boldsymbol{r}\alpha,\boldsymbol{r}'\alpha'}[\Sigma(\mathrm{i}\omega n)]_{\boldsymbol{r}\alpha,\boldsymbol{r}\alpha'}$.

(v) An $SU(2)$ Anderson impurity model (AIM) is considered to depict the local physics at position $\boldsymbol{r}$ on the lattice. The AIM is characterized by two sets of parameters: (i) real parameters $\varepsilon\boldsymbol{r}l$ representing the bath onsite energies, and (ii) complex $N\times N$ matrix parameters $V_l^{\boldsymbol{r}}$ describing the hopping from the bath to the impurity.

(vi) The AIM is subsequently diagonalized to yield the interacting Green function $\tilde{\boldsymbol{G}}(\mathrm{i}\omega n)$ at the impurity site using Lehmann representation.[35–37] The updated self-energy is then obtained via:

$$\sum_{\boldsymbol{r}}(\mathrm{i}\omega_n) = \tilde{g}^{(0)}(\mathrm{i}\omega_n)^{-1} - \tilde{g}(\mathrm{i}\omega_n)^{-1}. \tag{6}$$

We use Eq. (6) for the next iteration. These iterations will be continued until convergence is obtained. In our real-space DMFT (RDMFT) calculations, self-consistency is achieved when the change in the local self-energy between successive iterations falls below a relative threshold of 10^{-5}. We have verified the robustness of our solutions by starting from different initial self-energy configurations, including paramagnetic, antiferromagnetic, and random seeds. In all cases, the iteration converged to the same physical solution, indicating that our results are independent of the starting condition. Furthermore, to ensure numerical stability near phase boundaries, we adopt a continuation strategy: we start from a converged solution at large U and gradually decrease U in small steps, using the previous solution as the initial guess for the next step. This procedure helps to track magnetic solutions and avoid convergence to metastable states.

4. Topological properties of the model

The eigenstates of the non-interacting (NI) HHHH Hamiltonian are denoted as $|\boldsymbol{\lambda}-k\rangle$ and $|\boldsymbol{\lambda}+k\rangle$, which correspond to the lower and upper energy bands respectively. As long as $\Delta/t<2$, an energy gap between these bands exists, categorizing the system within the insulator phase. At $\Delta/t=2$, the two bands exhibit a touching point at $(k_X,k_Y):=(\pi/2,0)$ in the Brillouin zone (BZ), transitioning the system into a metallic phase. With a subsequent increase in Δ/t, the energy gap reopens, returning the system to another insulator phase. The question that arises is the distinction between these two insulator phases.

The Chern number is a topological invariant, remaining constant under smooth band deformations. It only changes if the bands touch, which occurs exclusively when the charge gap closes. In the context of topological insulators, we are aware that the non-trivial insulator phase with a Chern number $\neq 0$ can transition to a trivial insulator phase with a Chern number of 0, while the metallic phase exists as an intermediate state.[39] Thus, our objective is to compute the Chern number for the system in these insulator phases. The Chern numbers $C_\pm$ of the lower and upper bands described by $E_\pm(\boldsymbol{k})$ are calculated using the formula:

$$C^{\pm} = \frac{1}{2\pi}\int_{BZ} \mathrm{d}k_x, \mathrm{d}k_y \left[\boldsymbol{\nabla}\times\langle\lambda_{\boldsymbol{k}}^{\pm}|(-\mathrm{i}\boldsymbol{\nabla}_{\boldsymbol{k}})|\lambda_{\boldsymbol{k}}^{\pm}\rangle\right], \tag{7}$$

where k_x, $k_y\in BZ$. The system at half-filling is identified as an NI for $\Delta/t>2$, characterized by a Chern number $C_\pm=0$. Conversely, for $\Delta/t<2$, the system takes the form of a QHI with Chern number values of $C_\pm=\mp 2$.[40–42] Notably, the value of the Chern number for $\Delta/t<2$ depends on the gauge function, as it cannot be universally defined across the entire BZ. A particularly intriguing observation is that regardless of weak or strong NNN hopping ($t'/t=0.25, t'/t=1$), the metallic phase arises at $\Delta/t=2$. Figure 2 illustrates the variation in the Chern number with respect to Δ/t for $U/t=0$. When accounting for spin degree of freedom and considering both $\uparrow$ and $\downarrow$ spins in the lower band occupation, the Chern number of the half-filled system becomes:

$$C^{-} = C_{\uparrow}^{-} + C_{\downarrow}^{-} = +1+1 = +2. \tag{8}$$

The one-parameter phase diagram of the HHHH model is displayed in Fig. 2. The region $\Delta/t<2$ corresponds to the QHI phase with a Chern number of 2, while the range $\Delta/t>2$ signifies the NI phase with a Chern number of 0. This characterization remains consistent for both weak and strong NNN hopping.

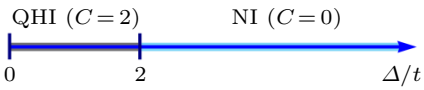


Fig. 2. The one-parameter phase diagram of the HHHH model. In $\Delta/t<2$ the phase of system is QHI with $C=2$, and in $\Delta/t>2$ the system is NI with $C=0$. This result is identical for weak and strong NNN hopping.

4.1. Chern number in the interacting model

The computation of the Chern number for interacting systems follows a methodology based on the topological Hamiltonian.[38] Remarkably, the Chern number of an interacting system equates to the Chern number of the ensuing NI Hamiltonian:

$$\hat{H}_{\mathrm{top}}(\boldsymbol{k}) = \hat{H}_0(\boldsymbol{k}) + \sum(\omega=0,\boldsymbol{k}), \tag{9}$$

here, $\Sigma(\omega=0,\boldsymbol{k})$ represents the self-energy of the interacting Hamiltonian at zero frequency, obtained through the RDMFT method. $\hat{H}_0(\boldsymbol{k})$ corresponds to the NI portion of the Hamiltonian in momentum space, derived from Eq. (1). In single-site DMFT, the self-energy lacks momentum dependence, i.e., $\Sigma(\omega=0,\boldsymbol{k})=\Sigma(\omega=0)$. In our model, two sub-lattices A and

B possess on-site energies of $+\Delta/t$ and $-\Delta/t$ respectively. Thus, the topological Hamiltonian takes the form of a 2×2 matrix:

$$\hat{H}_{\rm top}(\boldsymbol{k}) = \hat{H}_0(\boldsymbol{k}) + \begin{pmatrix} \Sigma_A(0) & 0 \\ 0 & \Sigma_B(0) \end{pmatrix} \tag{10}$$

Here, $\Sigma_A(0)$ and $\Sigma_B(0)$ denote the self-energy at sublattices A and B, respectively, at $\omega = 0$. An immediate consequence is that the paramagnetic phase for $\Delta/t = 0$ is always a QHI. We conclude that the one-parameter phase diagram for NI model and interacting model (paramagnetic phase) are similar to Fig. 2.

The magnetic order in Neél antiferromagnetic (AF) states aligned anti-parallel $'$ on the 4-unit cell atoms of the square lattice. The Neél AF $'$ of the model which can be shown schematically in Fig. 3(a) is invariant under translation by 2 sites along $\hat{x},\hat{y}$ axis. It has a unit cell of 4 sites (2×2). We have represented the 4 sites in the unit cell as ($A1$, $A2$, $B1$, $B2$). According to topological Hamiltonian approach[38] the effect of the selfenergy in the topological Hamiltonian is to modify only the onsite energies. The onsite energies of the 4 sites in the unit cell are given by

$$\begin{aligned}
(A_1)^\sigma: &\quad +\Delta + \sum_{A_1}^{\sigma}(\omega = 0),\\
(A_2)^\sigma: &\quad +\Delta + \sum_{A_2}^{\sigma}(\omega = 0),\\
(B_1)^\sigma: &\quad -\Delta + \sum_{B_1}^{\sigma}(\omega = 0),\\
(B_2)^\sigma: &\quad -\Delta + \sum_{B_1}^{\sigma}(\omega = 0).
\end{aligned} \tag{11}$$

The fundamental and pivotal invariant symmetry equation can readily be derived.

$$\sum_{X_1}^{\sigma}(0) = \sum_{X_2}^{\sigma}(0), \tag{12}$$

where X indicates sub-lattices $A(B)$. In the following, we define,

$$\sum_{X_\pm}^{\sigma}(0) = \frac{\Sigma_{X_1}^{\sigma}(0) + \Sigma_{X_2}^{\sigma}(0)}{2}. \tag{13}$$

We notice that according to Eq. (13), we have $\sum_{X\pm}^{\delta}(0) = \sum_{X\pm}^{\bar{\delta}}(0)$. Due to the symmetry relation Eqs. (12) and (13), we obtain new renormalized $\tilde{\Delta}$, δ_∂ for every sub-lattice. In addition to Eq. (14), we have also the following symmetry at zero frequency,[41,42]

$$\sum_{A_1}^{\sigma}(0) - \sum_{A_2}^{\sigma}(0) = \sum_{B_2}^{\sigma}(0) - \sum_{B_1}^{\sigma}(0), \tag{14a}$$

or

$$\sum_{A_-}^{\sigma}(0) = -\sum_{B_-}^{\sigma}(0). \tag{14b}$$

Using Eqs. (12)–(14) and straightforward calculations, the new renormalized onsite energies take the following forms,

$$\tilde{\Delta} = \Delta + \frac{\Sigma_{A_+}(0) - \Sigma_{B_+}(0)}{2}, \tag{15}$$

$$\delta_\sigma = \sum_{A_-}^{\sigma}(0). \tag{16}$$

Finally, the topological Hamiltonian can be rewritten for the spin component $\sigma = \uparrow, \downarrow$ for Neél AF as,

$$H_{\rm top}^{\sigma} = H_{\rm t}^{\sigma} + \sum_{\boldsymbol{r}} \left[\Delta(-1)^{x+y} + \delta_\sigma(-1)^{x+y}\right] n_{\boldsymbol{r}\sigma}, \tag{17}$$

where $H_{\rm t}$ is the hopping term and the effective potentials $\tilde{\Delta}$ and δ_∂, in the spirit of Refs. [45–47], are given by

$$\tilde{\Delta} = \Delta + \frac{1}{4}\left[\sum_{A_1}^{\sigma}(0) + \sum_{A_2}^{\sigma}(0) - \sum_{B_1}^{\sigma}(0) - \sum_{B_2}^{\sigma}(0)\right], \tag{18a}$$

$$\delta_\sigma = \frac{1}{4}\left[\sum_{A_1}^{\sigma}(0) - \sum_{A_2}^{\sigma}(0) - \sum_{B_1}^{\sigma}(0) + \sum_{B_2}^{\sigma}(0)\right], \tag{18b}$$

where $\Sigma_\sigma X(0)$ is the zero-frequency self-energy at the site X with spin σ. $\tilde{\Delta}$ is spin-independent and $\delta\uparrow = -\delta\downarrow$.

The phase diagram of Eq. (18) is symmetric with respect to $\tilde{\Delta}\to -\tilde{\Delta}$ and $\delta_\sigma \to -\delta_\sigma$ and hence we can focus on $\tilde{\Delta}$, $\delta > 0$. If we consider $\delta_\sigma = 0$, the obtained phase diagram is the same as in Fig. 2 with two bands. In $\tilde{\Delta}/t > 2$ the system is in a trivial NI phase with Chern number $C = 0$, and for $\tilde{\Delta}/t < 2$ we have a QHI phase with Chern number $C \neq 0$. This spatial anisotropy is a consequence of the staggered potential Δ. Consequently, distinct spin components may fall within different topological regions, leading to the emergence of a $C = 1$ AFQHI.

We now turn our attention to the scenario of substantial NNN hopping, specifically when $t' = t$. Under this condition, the Mott insulator (MI) phase takes the form of a stripe AF arrangement. The AF ordering materializes along the $\hat{x}$, direction, while the $\hat{y}$ direction sees ferromagnetic ordering, as illustrated in Fig. 3(b).

Within the unit cell, comprising four sites, the topological Hamiltonian for the case of $t' = t$ can be succinctly expressed as follows, up to an insignificant constant:

$$H_{\rm top} = H_{\rm t} + \sum_{\boldsymbol{r},\sigma} \Delta_\sigma(-1)^x n_{\boldsymbol{r},\sigma}. \tag{19}$$

Here, $H_{\rm t}$ denotes the standard kinetic term. The effective potential term, given by

$$\tilde{\Delta}_\sigma = \Delta + \frac{1}{2}\left(\sum_{A}^{\sigma}(0) - \sum_{B}^{\sigma}(0)\right), \tag{20}$$

accounts for the spin-dependent variations in the self-energy. The specific spin component σ is characterized as being in a quantum Hall state if $|\tilde{\Delta}_\partial| < 2t$, and it assumes a normal state if $|\tilde{\Delta}_\partial| > 2t$. As we show in Fig. 3(b), the stripe AF phase has transnational invariant by 1 site along $\hat{x} \pm \hat{y}$ axis if we perform a spinflip transformation.

It is apparent from Eq. (18a) that in this case the two spin components are always in the same topological state due to $\delta\uparrow = -\delta\downarrow$. This makes the emergence of a $C = 1$ stripe AF impossible. This can also be understood from the symmetry of the phase, without considering the topological Hamiltonian Eq. (19). In the stripe AF illustrated in Fig. 3(b), the effect of the spin-flip transformation can be compensated by a lattice translation, i.e., by a shift along $\hat{x}+\hat{y}$-direction. This suggests that spinup and spindown fermion dispersions will differ at most by a shift in momentum space.

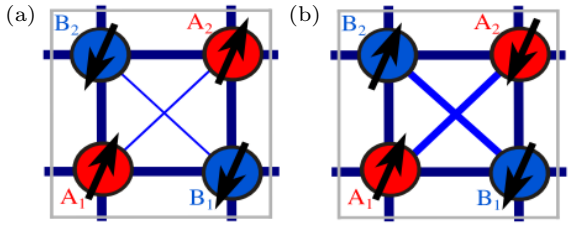


Fig. 3. The unit cell of the square lattice.

5. Effects of NNN hopping on the quantum phase transition

In this study we want to find the possible AFQHI with $C = 1$ in different NNN hopping limits. Therefore, we need to study the interacting model. In the following, we study the system in two different conditions: (i) the weak NNN hopping, $t'/t = 0.25$, (ii) the strong NNN hopping, $t'/t = 1$. We apply the RDMFT method for studying and calculation of phase transition of the system e.g. magnetization, double occupancy and renormalized staggered potential.

5.1. Weak NNN hopping

The magnetization, represented as $m = n\uparrow - n\downarrow$, and the double occupancy, denoted by $d = \langle n\uparrow n\downarrow\rangle$, hold considerable significance in the investigation of correlated systems. Changes in these two quantities serve as indicators of magnetic phase transitions.[43] Moreover, in optical lattice experiments, the double occupancy provides insights into the phase characteristics of systems.[44] Figure 4 portrays the variations of magnetization and double occupancy for the model across different values of Δ/t, specifically $\Delta/t = 0, 2$, with respect to U/t. Within the framework of RDMFT calculations, the process initiates with higher values of U and proceeds by decrementing U systematically.

The trend is evident: for larger U, magnetization increases due to the enhanced repulsion effects between electrons, leading to heightened magnetization while diminishing double occupancy. These observations align with the calculated results and the substantial spin per site magnitude, indicating that the system resides in an AF phase for large U. Conversely, in high U, the double occupancy tends to be minimal.

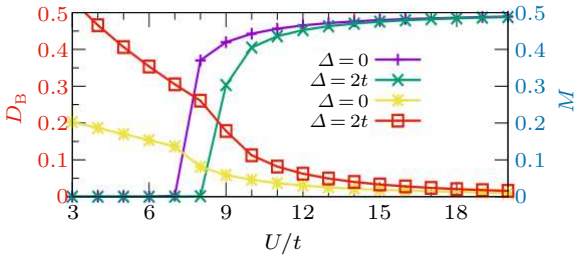


Fig. 4. $t' = 0.25t$; Magnetization and double occupancy plotted against U/t for different values of $\Delta/t = 0, 2$. The critical U for $\Delta/t = 0, 2$ are $Uc/t \approx 7.0, 8.0$, respectively.

Upon reducing the repulsion potential at the critical point U_c, the magnetization experiences a steep decline, signifying the transition to the paramagnetic phase. Notably, the double occupancy curve vs. U/t exhibits a discontinuity at U_c, followed by a subsequent increase at a constant rate. By comparing $\Delta = 0$ and $\Delta = 2t$, it becomes evident that increasing Δ/t results in a corresponding elevation of the critical U_c.

In Fig. 5, we present graphical representations of the local magnetic moment denoted as $M$and the effective potential represented as $\tilde{\Delta}_\partial$, both plotted against the parameter U. The dashed lines located at $\tilde{\Delta}_\partial = 2t$ and $\tilde{\Delta}_\partial = 2t$ establish the boundaries that define the region of interest characterized by $|\tilde{\Delta}_\partial| < 2t$. An area shaded in color indicates a phase possessing a finite Chern number C, which plays a crucial role in the analysis.

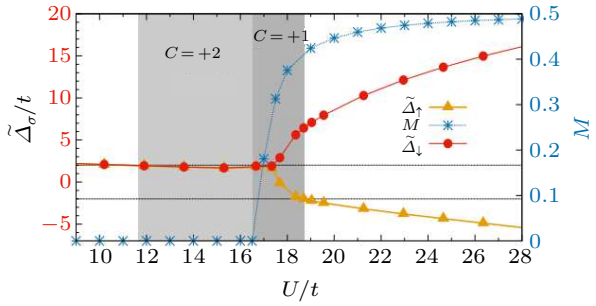


Fig. 5. The renormalized $\tilde{\Delta}$ for spinup and spin-down and magnetization vs. U/t are plotted for $\Delta/t = 7$.

We choose $t'/t = 0.25$ as a representative weak NNN hopping strength, which is commonly used in the literature to open a topological gap without suppressing interaction effects. This value ensures the Harper–Hofstadter bands are gapped while still allowing for strong-coupling phases such as the Mott and AFQHI states to emerge. In our calculations for $t'/t = 0.25$, we find that the $C = 1$ Neél AFQHI phase emerges in the intermediate interaction regime, approximately for $16.5 \lesssim U/t \lesssim 18.8$, as indicated by the gray-shaded region in Fig. 5. Notably, this $C = 1$ phase disappears when

$t'/t = 1$, where the symmetry constraints prevent the formation of a Neél AFQHI state.

Observing Fig. 5, it becomes apparent that with an increase in the value of U, the effective potential $\tilde{\Delta}_\partial$ experiences a reduction below $2t$ around the point $U \simeq 11.8t$, leading to a transition from a non-interacting (NI) state to a QHI state.

As U exceeds approximately $16.5t$, the local magnetic moment exhibits finiteness, and concurrently, $\tilde{\Delta}_\partial$ becomes spin-specific. Notably, one of the spin components (as illustrated by the downward-pointing arrow in the figure) swiftly exits the topological region, while the other spin component sustains its topological nature until roughly $U \simeq 18.8t$ as reported in Ref. [41]. This remarkable behavior gives rise to a distinctive phase, identified as a Neél AFQHI possessing a Chern number $C = 1$, for values of U within the range of $1t6.5 \lesssim U \lesssim 18.8t$.

Within the context of the Neél antiferromagnetic configuration presented in Fig. 3(a), it is crucial to note that the consequences of the spin-flip transformation are distinct from those observed in the stripe AF configuration. Consequently, both the spin-up and spin-down components possess the capacity to alter their respective Chern numbers at distinct transition points. This intricate behavior culminates in the emergence of the $C = 1$ Neél AFQHI.

The emergence of the $C = 1$ phase can be understood by examining the spin-resolved response of the system in the presence of Neél antiferromagnetic ordering. In this configuration, the spin-up and spin-down components experience different effective potentials due to the staggered magnetization. As a result, the two spin sectors can undergo topological transitions at different interaction strengths. Specifically, in the intermediate U/t range, one spin component (e.g., spin-up) may remain in a topologically nontrivial quantum Hall phase while the other (e.g., spin-down) becomes trivial. This spin-selective behavior is reflected in Fig. 5, where the down-arrow marks the point at which the spin-down component loses its topological character. The system then enters a Chern insulating phase with

$C = 1$, contributed solely by the spin-up band. As U increases further, the staggered magnetization becomes stronger, polarizing the system such that both spin sectors eventually transition into trivial insulating states, thereby destroying the $C = 1$ phase. This behavior highlights the delicate balance between spin polarization and band topology in determining the stability of interaction-driven topological phases.

5.2. Strong NNN hopping

In this section, we consider $t' = t$ as a strong NNN hopping term. According to Fig. 1, the NNN hopping in diagonal directions, are different because of dependency to x position of atoms, but the norm of NNN hopping in $\hat{x} - \hat{y}$ and $\hat{x} + \hat{y}$ direction are same. The numerical results for the strong hopping parameter changed the magnetic order. We found that for large U, the magnetic order is stripe antiferromagnetic (SAF), the atoms in sub-lattice A have spin up and in B sublattice have spin down.

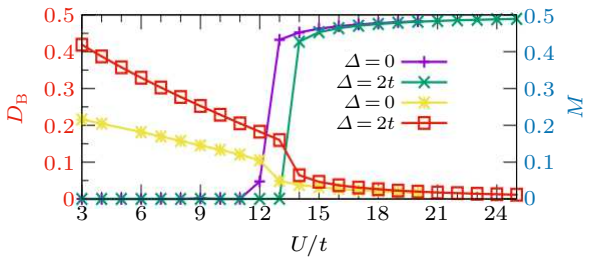


Fig. 6. $t' = t$; Magnetization and double occupancy plotted against U/t for different values of $\Delta/t = 0$, 2. The critical U for $\Delta/t = 0$ is $Uc/t \approx 11.0$ and $Uc/t \approx 13.0$, respectively.

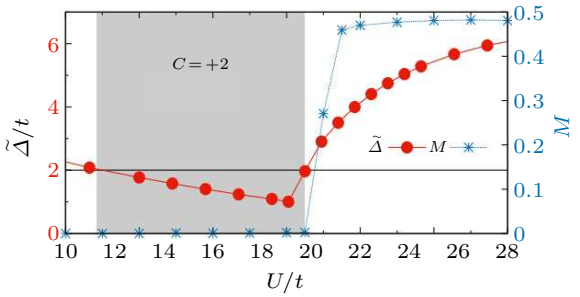


Fig. 7. The magnetization and $\tilde{\Delta}$ for spinup and spin-down are plotted vs. U. We considered $\Delta = 7t$. The QHI region is plotted with $C = +2$.

In Fig. 7, the magnetization and $\tilde{\Delta}/t$ vs. U are plotted. In Fig. 7 we considered the $\Delta = 7t$, in $-2 \leq \tilde{\Delta}/t \leq 2$ we found only one phase, a QHI ($C = +2$) phase. As we can see, both spin compnanets have the same topological phase.

In the regime where $\Delta = 7t$ and U is small, both spinup and spin-down states reside in the NI phase. As the repulsion potential increases, specifically at $U \approx 16.9t$, both states transition to the QHI phase characterized by a Chern number of 2. At $U \approx 22.5t$, the system exhibits a zero magnetization, leading it to adopt a stripe AF configuration.

While our results are presented for two representative limits, $t'/t = 0.25$ (weak NNN hopping) and $t'/t = 1$ (strong NNN hopping), we expect the system to exhibit a continuous evolution of phases as t'/t varies between these two extremes. For intermediate values of t'/t, the boundaries between the trivial insulator, $C = 1$ Neél AFQHI, and other magnetic phases would shift accordingly. Based on our symmetry analysis, the emergence of the $C = 1$ phase requires that the spin-flip transformation cannot be compensated by a space-group operation, a condition that is satisfied only when the NNN hopping is sufficiently strong to lift the symmetry constraints. Therefore, a finite but moderate t'/t is necessary to stabilize the $C = 1$ Neél AFQHI phase, while too large a value of t'/t favors a transition to stripe ordering instead. We anticipate that the region of the $C = 1$ phase shrinks and eventually vanishes as t'/t in-

creases beyond a certain threshold, consistent with our results at $t'/t = 1$, where this phase is absent.

6. Conclusion

We have conducted an in-depth analysis of the HHHH model within a square optical lattice framework. Initially, we adopted the topological Hamiltonian methodology to investigate the topological characteristics of the system under interaction. The results obtained from the real-space DMFT approximation informed our analysis. We charted the topological phase transition concerning renormalized parameters Δ and δ.

For a specific condition, $\Delta = 7t$, the AFQHI phase with a Chern number of $+1$ emerges as an intermediate phase, positioned between the NI phase ($C = 0$) and the QHI phase with $C = 2$. Additionally, the QHI phase with a Chern number of $+2$ appears sandwiched between two instances of the NI phase, both having a Chern number of 0.

Subsequently, we delved into the influence of NNN hopping on the model's phase diagram. We computed the system's magnetization as order parameters across diverse magnitudes of Δ and U to discern the magnetic phase transitions. The parameter $\tilde{\Delta}$ was derived for dual spin elements. In the presence of pronounced NNN hopping, we identified the stripe-AFI phase and discerned the existence of the QHI as an intermediary phase adjacent to the NI phase.

It is noteworthy that our inference regarding the plausible presence of a $C = 1$ AFQHI stems from the phase's symmetry rather than intricate model details addressed in this work. Introducing a staggered potential, given by H_Δ which varies along both $\hat{x}$ and $\hat{y}$ axes, would culminate in a $C = 1$ Neél, thereby inhibiting a $'C = 1$ stripe AFQHI. Our deductions align with the observations related to the $C = 1$ AFQHI in the Haldane–Hubbard model.[22,23] Our findings offer valuable insights, potentially directing forthcoming experimental endeavors, notably within optical lattice setups, in the pursuit of AFQHI phases.

References

[1] Cooper N R, Dalibard J and Spielman I B 2019 *Rev. Mod. Phys.* **91** 015005
[2] Aidelsburger M, Nascimbene S and Goldman N 2018 *C. R. Physique* **19** 394
[3] Mazurenko A, Chiu C S, Ji G, Parsons M F, Kanasz-Nagy M, Schmidt R, Grusdt F, Demler E, Greif D and Greiner M 2017 *Nature* **545** 462
[4] Brown P T, Mitra D, Guardado-Sanchez E, Schauß P, Kondov S S, Khatami E, Paiva T, Trivedi N, Huse D A and Bakr W S 2017 *Science* **357** 1385
[5] Hofstetter W and Qin T 2018 *J. Phys. B: At. Mol. Opt. Phys.* **51** 082001
[6] Miyake H, Siviloglou G A, Kennedy C J, Butron W C and Ketterle W 2013 *Phys. Rev. Lett.* **111** 185302
[7] Aidelsburger M, Lohse M, Schweizer C, Atala M, Barreiro J T, Nascimbene S, Cooper N R, Bloch I and Goldman N 2015 *Nat. Phys.* **11** 162
[8] Aidelsburger M, Atala M, Nascimbene S, Trotzky S, Chen Y A and Bloch I 2011 *Phys. Rev. Lett.* **107** 255301
[9] Köhler T, Góral K and Julienne P S 2006 *Rev. Mod. Phys.* **78** 1311
[10] Eckardt A, Weiss C and Holthaus M 2005 *Phys. Rev. Lett.* **95** 260404
[11] Lignier H, Sias C, Ciampini D, Singh Y, Zenesini A, Morsch O and Arimondo E 2007 *Phys. Rev. Lett.* **99** 220403
[12] Zenesini A, Lignier H, Ciampini D, Morsch O and Arimondo E 2009 *Phys. Rev. Lett.* **102** 100403
[13] Hemmerich A 2010 *Phys. Rev. A* **81** 063626
[14] Struck J, Olschläger C, Weinberg M, Hauke P, Simonet J, Eckardt A, Lewenstein M, Sengstock K and Windpassinger P 2012 *Phys. Rev. Lett.* **108** 225304
[15] Duncan R 1976 *Phys. Rev. B* **14** 2239
[16] Hatsugai Y and Kohmoto M 1990 *Phys. Rev. B* **42** 8282
[17] Jiang K, Zhou S, Dai X and Wang Z 2018 *Phys. Rev. Lett.* **120** 157205
[18] Arun V S, Sohal R, Hickey C and Paramekanti A 2016 *Phys. Rev. B* **93** 115110
[19] Haldane F D M 1988 *Phys. Rev. Lett.* **61** 2015
[20] Beugeling W, Everts J C and Morais Smith C 2012 *Phys. Rev. B* **86** 195129
[21] Hatsugai Y and Kohmoto M 1990 *Phys. Rev. B* **42** 8282
[22] He J, Zong Y H, Kou S P, Liang Y and Feng S 2011 *Phys. Rev. B* **84** 035127
[23] Vanhala T I, Siro T, Liang L, Troyer M, Harju A and Törmä P 2016 *Phys. Rev. Lett.* **116** 225305
[24] Tupitsyn I S and Prokofév N V 2019 *Phys. Rev. B* **99** 121113
[25] Ebrahimkhas M 2011 *Phys. Lett. A* **375** 3223
[26] Shahbazy A and Ebrahimkhas M 2019 *Chin. J. Phys.* **58** 273
[27] Cocks D, Orth P P, Rachel S, Buchhold M, Le Hur K and Hofstetter W 2012 *Phys. Rev. Lett.* **109** 205303
[28] Irsigler B, Zheng J H and Hofstetter W 2019 *Phys. Rev. Lett.* **122** 010406
[29] Goldman N, Juzeliūnas G, Öhberg P and Spielman I B 2014 *Rep. Prog. Phys.* **77** 126401
[30] Potthoff M and Nolting W 1999 *Phys. Rev. B* **59** 2549
[31] Song Y, Wortis R and Atkinson W A 2008 *Phys. Rev. B* **77** 054202
[32] Zheng J H, Qin T and Hofstetter W 2019 *Phys. Rev. B* **99** 125138
[33] Orth P P, Cocks D, Rachel S, Buchhold M, Hur K L and Hofstetter W 2013 *J. Phys. B: At. Mol. Opt. Phys.* **46** 134004
[34] He L, Ji A and Hofstetter W 2015 *Phys. Rev. A* **92** 023630
[35] Hafez-Torbati M and Hofstetter W 2018 *Phys. Rev. B* **98** 245131
[36] Hafez-Torbati M and Hofstetter W 2019 *Phys. Rev. B* **100** 035133
[37] Snoek M, Titvinidze I, Toke C, Byczuk K and Hofstetter W 2008 *New J. Phys.* **10** 093008
[38] Wang Z and Zhang S C 2012 *Phys. Rev. X* **2** 031008
[39] Fruchart M and Carpentier D 2013 *C. R. Physique* **14** 779
[40] Kohmoto M 1985 *Ann. Phys.* **160** 343
[41] Ebrahimkhas M, Hafez-Torbati M and Hofstetter W 2021 *Phys. Rev. B* **103** 155108
[42] Ebrahimkhas M, Uhrig G S, Hofstetter W and Hafez-Torbati M 2023 *Phys. Rev. B* **106** 205107
[43] van Loon E G C P, Krien F, Hafermann H, Stepanov E A, Lichtenstein A I and Katsnelson M I 2016 *Phys. Rev. B* **93** 155162
[44] Strohmaier N, Greif D, Ördens R J, Tarruell L, Moritz H and Esslinger T 2010 *Phys. Rev. Lett.* **104** 080401
[45] Hafez-Torbati M, Zheng J H, Irsigler B and Hofstetter W 2020 *Phys. Rev. B* **101** 245159
[46] Amaricci A, Budich J C, Capone M, Trauzettel B and Sangiovanni G 2015 *Phys. Rev. Lett.* **114** 185701
[47] Crippa L, Amaricci A, Wagner N, Sangiovanni G, Budich J C and Capone M 2020 *Phys. Rev. Res.* **2** 012023
[48] Golubeva A, Sotnikov A and Hofstetter W 2015 *Phys. Rev. A* **92** 043623